

PAPER • OPEN ACCESS

Characterization of magnetic interference and image artefacts during simultaneous in-beam MR imaging and proton pencil beam scanning

To cite this article: Sebastian Gantz *et al* 2020 *Phys. Med. Biol.* **65** 215014

View the [article online](#) for updates and enhancements.

You may also like

- [Monte Carlo study of the potential reduction in out-of-field dose using a patient-specific aperture in pencil beam scanning proton therapy](#)

Stephen J Dowdell, Benjamin Clasie, Nicolas Depauw et al.

- [Liquid Crystal Alignment on Plasma Beam Scanned Alkylsiloxane Self-Assembled Monolayers](#)

K. Y. Wu, W. Y. Chen, C.-H. Wang et al.

- [Proton pencil beam scanning for mediastinal lymphoma: the impact of interplay between target motion and beam scanning](#)

C Zeng, J P Plastaras, Z A Tochner et al.



OPEN ACCESS

RECEIVED
15 April 2020

REVISED
5 August 2020

ACCEPTED FOR PUBLICATION
21 August 2020

PUBLISHED
4 November 2020

Original content from
this work may be used
under the terms of the
[Creative Commons
Attribution 4.0 licence](#).

Any further distribution
of this work must
maintain attribution to
the author(s) and the title
of the work, journal
citation and DOI.



PAPER

Characterization of magnetic interference and image artefacts during simultaneous in-beam MR imaging and proton pencil beam scanning

Sebastian Gantz^{1,2} , Volker Hietschold³ and Aswin Louis Hoffmann^{1,2,4,5}

¹ OncoRay—National Center for Radiation Research in Oncology, Faculty of Medicine and University Hospital Carl Gustav Carus, Technische Universität Dresden, Helmholtz-Zentrum Dresden–Rossendorf, Dresden, Germany

² Institute of Radiooncology—OncoRay, Helmholtz-Zentrum Dresden–Rossendorf, Dresden, Germany

³ Department of Radiology, Faculty of Medicine and University Hospital Carl Gustav Carus, Technische Universität Dresden, Dresden, Germany

⁴ Department of Radiotherapy and Radiation Oncology, Faculty of Medicine and University Hospital Carl Gustav Carus, Technische Universität Dresden, Dresden, Germany

⁵ Author to whom any correspondence should be addressed.

E-mail: Aswin.Hoffmann@uniklinikum-dresden.de

Keywords: MRI, proton therapy, image quality, pencil beam scanning, magnetometry

Abstract

For the first time, a low-field open magnetic resonance (MR) scanner was combined with a proton pencil beam scanning (PBS) research beamline. The aim of this study was to characterize the magnetic fringe fields produced by the PBS system and measure their effects on MR image quality during simultaneous PBS irradiation and image acquisition. A magnetic field camera measured the change in central resonance frequency (Δf_{res}) and magnetic field homogeneity (ΔMFH) of the B_0 field of the MR scanner during operation of the beam transport and scanning magnets. The beam energy was varied between 70 – 220 MeV and beam scanning was performed along the central horizontal and vertical axis of a $48 \times 24 \text{ cm}^2$ radiation field. The time structure of the scanning magnets' fringe fields was simultaneously recorded by a tri-axial Hall probe. MR imaging experiments were conducted using the ACR (American College of Radiology) Small MRI Phantom and a spoiled gradient echo pulse sequence during simultaneous volumetric irradiation. Computer simulations were performed to predict the effects of B_0 field perturbations due to PBS irradiation on MR image formation in k -space. Setting the beam transport magnets, horizontal and vertical scanning magnets resulted in a maximum Δf_{res} of 50, 235 and 4 Hz, respectively. The ΔMFH was less than 3 parts per million for all measurements. MR images acquired during beam energy variation and vertical beam scanning showed no visual loss in image quality. However, MR images acquired during horizontal beam scanning showed severe coherent ghosting artefacts in phase encoding direction. Both simulated and measured k -space phase maps prove that these artefacts are caused by phase-offsets. This study shows first experimental evidence that simultaneous in-beam MR imaging during proton PBS irradiation is subject to severe loss of image quality in the absence of magnetic decoupling between the PBS and MR system.

1. Introduction

Real-time magnetic resonance imaging (MRI) guidance is expected to improve the targeting precision of proton therapy (PT), in particular for soft-tissue tumors that move during dose delivery (Oborn *et al* 2017). However, hybrid systems for MR-integrated PT (MRiPT) do not exist due to a number of hitherto open technological questions, such as beam delivery inside the complex-shaped magnetic fringe field of an MR scanner and the mutual magnetic interactions of both systems, which potentially degrade both the beam and image quality (Schippers and Lomax 2011). In a previous study we have shown that the integration of a low-field open MRI scanner with a static proton research beam line is technically feasible without

introducing severe degradation in MR image quality during simultaneous irradiation (Schellhammer *et al* 2018a). However, dose delivery at such a static beam line is limited to passive scattering, which is considered not to be a feasible method for beam delivery in magnetic fields of an MR scanner, because the polyenergetic beams will be spatially degraded as they are transported towards the imaging volume of the MRI scanner (Oborn *et al* 2015). Furthermore, active pencil beam scanning (PBS) is considered the state-of-the-art technique for modern clinical PT facilities.

We therefore recently realized a setup of a first prototype *in-beam* MRI scanner at a PBS research beam line producing actively scanned beams of clinical quality. This PBS beam line consists essentially of two types of magnets. Firstly, quadrupole electromagnets are used for beam transport and focusing. The electrical current that energizes these magnets depends on the requested beam energy or range. Secondly, a pair of dipole scanning electromagnets (Schippers 2018) is used to dynamically steer the beam in two lateral directions perpendicular to the central beam axis. Three-dimensional (3D) volumetric irradiation is then achieved stepwise in layers of equal proton beam energy (or range), while the dose is delivered by simultaneously controlling the beam spot intensity (*i.e.* dose per spot) and the spot position in both lateral directions (Marchand *et al* 2000).

Both static and dynamic magnetic fringe fields are produced by the PBS beam line and scanning magnets during operation. As these are likely to overlap with the magnetic field deployed for imaging by the *in-beam* MRI scanner, magnetic interference is expected to distort the MR imaging field and hence degrade the MR image quality during PBS irradiation. To the best of our knowledge, only a single simulation study (Oborn *et al* 2016) exists which investigated MRI and scanning magnet cross-talk during proton PBS irradiation in a hypothetical MRiPT system and concluded that MR image quality is maintained during PBS irradiation with adequate shimming. However, this study only investigated the effects of the dynamic fringe field of the scanning magnets on the homogeneity of the static magnetic field of the MR scanner and experimental data confirming these results are lacking to date.

Therefore, the aim of this study was to assess the magnetic field effects of the static and dynamic fringe field components of the PBS beam line magnets onto the static and dynamic magnetic fields of the MRI scanner. For this purpose, we utilized both direct magnetic field measurements to characterize the magnetic field homogeneity (MFH) and the central resonance frequency of the static (B_0) magnetic field, as well as MR imaging experiments to characterize the image quality during simultaneous operation of the PBS beam line. Additionally, we substantiate our experimental findings by theoretical considerations and computer simulations of the MR image acquisition process under non-stationary magnetic field effects.

2. Materials and methods

2.1. Measurement setup

A C-shaped open MRI scanner (MrJ2200, ASG Superconductors S.p.A., Genua, Italy) based on a 0.22 T Nd₂Fe₁₄B permanent magnet was combined with a horizontal dedicated PBS nozzle (IBA Particle Therapy, Louvain-la-Neuve, Belgium) at a research beam line that is connected to an isochronous cyclotron (C230, Ion Beam Applications SA, Louvain-la-Neuve, Belgium). The MRI scanner was enclosed by a Faraday cage made of plywood panels laminated with a 120 μm thick copper foil (figure 1) to shield the MRI scanner from external radiofrequency (RF) sources of the PT facility. Further details about the MRI scanner have been published in (Schellhammer *et al* 2018a). The MRI scanner utilizes a vertically upwards directed B_0 field (positive Y axis) in the field-of-view (FOV) that is perpendicular to the central beam axis (positive Z axis). The scanner was positioned in front of the PBS beamline such that the iron flux return yoke is on the left lateral side in beams-eye-view, and the beam incident to the MR imaging field is deflected to the right lateral side (negative X axis), thus minimizing the potential risk of directly activating the yoke material by incident protons. The scanner was positioned with the MR isocenter on the central beam axis and as close as possible to the PBS nozzle to minimize beam widening by air scattering, resulting in a distance of MR isocenter to beam-exit window of 1.02 m.

The horizontal (X) and vertical (Y) scanning magnets are positioned downstream from the last quadrupole magnets (2.99 m from MR isocenter), at a distance of 2.33 and 2.73 m from the MR isocenter, respectively (figure 1). To prevent demagnetization effects, the maximum irradiation field size at the MR isocenter was restricted to 48 cm and 24 cm in X and Y direction, respectively, in order not to hit and activate the flux return yoke or the magnet poles (Ito *et al* 2001).

2.2. Magnetic field measurements

To characterize the effects of the fringe fields of the PBS beam line on the B_0 field of the MRI scanner a magnetic field camera (MFC3045, Metrolab, Geneva, Switzerland) was centrally positioned at the MR isocenter. A standard half-moon type probe array with a nominal radius of 11 cm was used. Sixteen probes

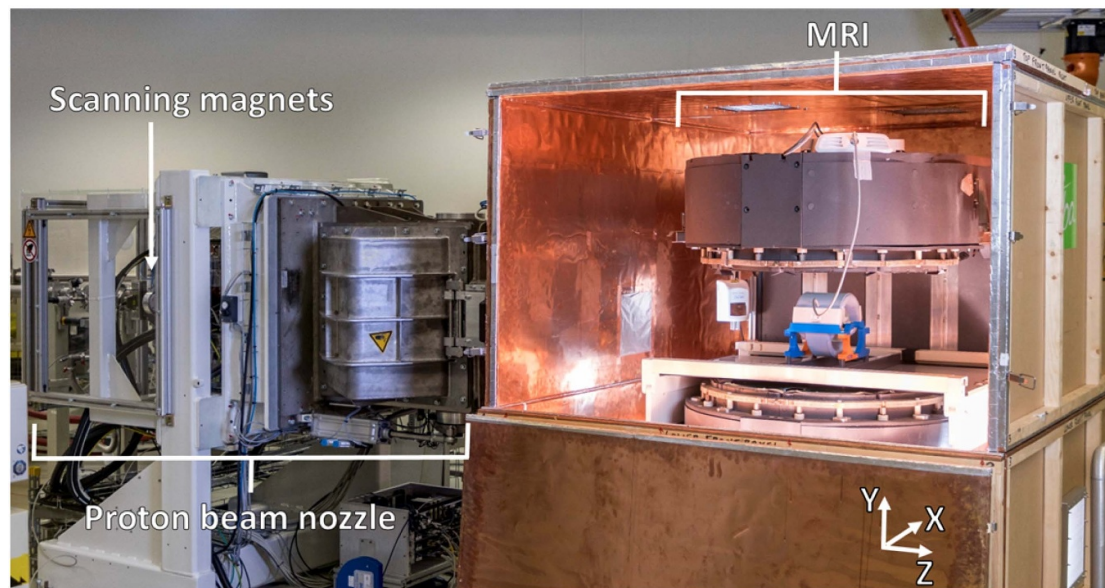


Figure 1. Experimental setup with opened Faraday cage. The *in-beam* MR scanner is positioned directly in front of the proton PBS nozzle, which houses the X and Y beam scanning magnets. [Courtesy of HZDR/R.Weisflog].

were evenly distributed along the arc of a half circle. Each probe measured the resonance frequency at a specific location. The probe array was manually rotated along the B_0 field axis at 12 steps of 30° each. For a full rotation, in total 16×12 samples were acquired on the surface of a 22 cm diameter-spherical volume. From this data, both the central resonance frequency (f_{res}), which was the average frequency over all 192 samples, and the peak-to-peak frequency variation relative to the central resonance frequency to indicate the MFH were calculated. Due to the need for manual rotation and a measurement time of about 5 s per position, the field camera could only be used to measure the static fringe field effects of the PBS beam line and scanning magnets on the B_0 field of the MRI scanner.

Since the current settings of the beam transport magnets and the scanning magnets are related to the requested beam energy and the spot position, respectively, two magnetometry experiments were conducted with the magnetic field camera. Firstly, the fringe field effects of the quadrupole magnets on the B_0 field were measured for a series of central spot irradiations at four different energies (70, 125, 170, 220 MeV), covering the clinical range of proton energies at our facility. Secondly, the fringe field effects of the dipole scanning magnets on the B_0 field were measured for two extreme spot positions along both vertical ($Y = \pm 12$ cm) and horizontal ($X = \pm 24$ cm) axis at a fixed energy of 220 MeV. To prevent the camera from being irradiated, all magnets of the PBS beam line were energized without the beam being transported. Moreover, this allowed all magnets to be energized to the specified current settings for each individual spot for a suitable time (2 min) in order to manually rotate the camera over 360 degrees. All measurements were repeated three times in succession with baseline measurements using non-energized magnets in between, to compensate for the magnetic field drift that may occur due to environmental temperature changes in the permanent magnets of the MRI scanner (Li *et al* 2009, Huang *et al* 2018).

To enable the measurement of dynamic fringe field effects produced by the beam line and scanning magnets, a tri-axial Hall probe (THM1176LF, Metrolab, Geneva, Switzerland) was placed laterally from the center of the Y scanning magnet at 70 cm perpendicular to the central beam axis. This allowed for fast logging of the fringe field up to 500 Hz. For all dynamic imaging experiments (section 2.3.2), 3D magnetic fringe field data was acquired using the coordinate system described above. Measured field data is reported as the difference compared to the baseline scenario in which all beam line and scanning magnets were disabled.

2.3. Image quality experiments

To characterize the effects of both the static and the dynamic fringe fields produced by the PBS beam line on the MR image quality, images were acquired of the American College of Radiology (ACR) Small Phantom (ACR Small MRI Phantom, Newmatic Medical, Grand Rapids, USA), being positioned centrally in a dedicated knee receiver coil at the magnetic isocenter. An in-house built coil and phantom holder were used for reproducible positioning thereof (Schellhammer *et al* 2018a).

A spoiled gradient echo sequence (GRE) (TE = 20 ms, TR = 80 ms, FA = 60° , FOV = 20×20 cm 2 , asymmetric sampling = 12.5%, phase encoding dummies = 25, acquisition matrix = 281 \times 314, Cartesian

sampling, reconstructed image = 256×256 , bandwidth = 42 Hz px^{-1}) was used to image a single transversal slice in the fluid-only region of the ACR phantom that is regularly used to quantify the image intensity uniformity and the percent signal ghosting (American College of Radiology 2008). The GRE sequence was preceded by a pre-scan frequency calibration in order to compensate for image shifts due to the thermal drift of B_0 . The total scan time of the GRE sequence excluding the pre-scan frequency calibration while including the phase encoding (PE) dummies was 22 s. The PE dummy scans were 25 repetitions of the first line of k -space, which were acquired in order to assure system phase stability and were discarded during image reconstruction.

The GRE sequence offered a reasonable compromise between image quality and acquisition speed, but was chosen primarily because of the simple sequence structure, which helped to unravel and understand the origin of potential imaging artefacts.

Operation of the proton beam line in PBS mode is a two-stage process. First, the current in the quadrupole magnets is set for the requested beam energy (and range). Then the scanning magnets are dynamically energizing to consecutively deliver the beam spots in a pre-defined pattern within the energy layer. To investigate the impact of these steps on the MR image quality, two experiments were conducted. First, a baseline experiment was conducted to assess the effect of setting only the beam line magnets. In the second experiment, the effect of volumetric PBS irradiation was assessed.

2.3.1. Baseline experiment: static beam line settings.

To test the hypothesis that setting the beam line magnets shows no visible effect on the MR image quality, image acquisition was performed both with the beam line magnets disabled or energized. For the latter, the magnet currents were set for a beam energy of 70, 125 and 220 MeV, without the beam being transported. The scanning magnets were not energized for this experiment.

2.3.2. Imaging and simultaneous volumetric proton beam scanning.

To test the hypothesis that the dynamic operation of the beam line and scanning magnets during simultaneous MR image acquisition affects the image quality, we decomposed the 3D volumetric radiation field into its three components: change of energy layers (Z), horizontal (X) and vertical scanning (Y). The energy variation was achieved by nine energy layers using beam energies from 220 MeV to 140 MeV, with equidistant decreasing energy steps of 10 MeV and a single central spot for each layer. The corresponding spot map is indicated as Z9 in the following. For both lateral scanning directions, the central X and Y axis of a 48×24 cm radiation field were scanned individually using either 9, 17, 33 or 81 equidistant spot locations. The corresponding spot maps are designated as X9, X17, X33, X81 and Y9, Y17, Y33 and Y81 in the sequel. Each of the spot maps was designed such that the total dose delivery time was 20 s. In this way dose delivery was completed within the image acquisition time frame, while starting after the pre-scan frequency calibration to make sure the latter is not affected by dynamic beam scanning effects. To test for reproducibility, all experiments were repeated three times. The MR image quality was evaluated qualitatively and compared to the images acquired for the baseline experiment.

2.4. Theory and computer simulation

Under the hypothesis that the dynamic fringe fields of the beam line and scanning magnets change the B_0 field of the MR scanner during image acquisition, implications for the data acquisition in k -space and the reconstructed MR images can be deduced from theoretical considerations. From textbooks (Haacke *et al* 1999) it is well-known that the accumulated phase at time t after initial excitation of a detected MR signal can be expressed as:

$$\Delta\Phi(t, \mathbf{r}) = \gamma \int_0^t \Delta B_0(\tau, \mathbf{r}) d\tau,$$

where $\Delta B_0(\tau, r)$ is the change in the magnetic field strength, $T = 0$ is the time of the RF excitation, γ is the reduced gyromagnetic ratio for protons (42.6 MHz T^{-1}) and \mathbf{r} is the position vector.

If it is assumed that the change in the B_0 field is uniform over the whole FOV and time-invariant between the initial excitation and the time of the signal echo (TE), then $\Delta\Phi$ simplifies to

$$\Delta\Phi(t) = \gamma \Delta B_0 t = \Delta f t,$$

where Δf represents a change in central resonance frequency. Hence, a change in B_0 that occurs between two adjacent lines of k -space can be modelled as a phase ramp along the frequency encoding (FE) direction.

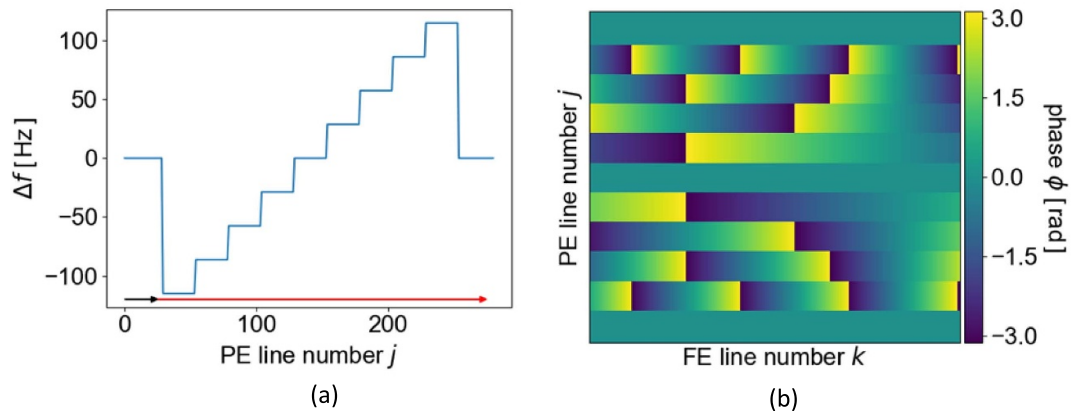


Figure 2. (a) Change in central resonance frequency as a function of PE line number j in k -space, as implemented for the simulation experiment. Black and red arrows indicate the time interval of the dummy scans and the actual image acquisition, respectively. (b) Resulting phase ramp matrix $M(k,j)$ for the simulation experiment.

Table 1. Change in central resonance frequency (Δf_{res}) as function of setting the beam line transport magnets to different proton energies.

Energy (MeV)	70	125	170	220
Δf_{res} (Hz)	18.0 ± 0.4	25.4 ± 0.4	32.3 ± 0.3	50.4 ± 0.5

The acquired phase error corrupted signal $S'(k,j)$ for PE line j is then given by (Durand *et al* 2001):

$$S'(k,j) = S(k,j) e^{i\Delta\Phi(t)} = S(k,j) e^{i\Delta f(j) t_k},$$

where $S(k,j)$ is the theoretical, uncorrupted signal, k is the sample number along FE direction and t_k is the time between RF excitation and sampling of the k th point along FE direction. In order to resemble the time structure of the X9 spot map from the simultaneous imaging and irradiation experiments (section 2.3.2), $\Delta f(j)$ was modelled as a function of PE line j using a maximum central resonance frequency change of $\Delta f = 230$ Hz (input taken from results of section 3.1), split into nine equidistant spots, *i.e.* in steps of $230/8 = 28.75$ Hz from -115 to $+115$ Hz, (figure 2(a)). Further, along FE direction, t_k was modelled using the precise timing of the GRE sequence, with a dwell time $t_d = 94.7 \mu\text{s}$ between sample points, that resulted from the sampling receiver bandwidth of the GRE sequence ($\text{rBW} = 10\,563$ Hz). This resulted in the phase ramp matrix $M(k,j) = e^{i\Delta f(j) t(k)}$ shown in figure 2(b). Furthermore, the k -space of a GRE image acquired during the baseline experiment was used as an approximation of the uncorrupted signal $S(k,j)$. In other words, the phase ramp matrix $M(k,j)$ was multiplied by the baseline k -space image. The reconstructed image resulting from the computer simulation in k -space was qualitatively compared to images acquired during the X9 beam-scanning experiments.

3. Results

3.1. Magnetic field measurements

3.1.1. Magnetic field camera.

The effect of the ambient temperature induced B_0 field drift was compensated by subtraction of a linear function that was fitted to the measurements of the baseline experiments. The mean frequency drift for all experiments was in the range from -0.1 to -0.5 Hz min^{-1} .

The measurements showed that the central resonance frequency monotonically increased with beam energy over a range from 18 to 50 Hz when the quadrupole magnets were set to the energy range from 70 to 220 MeV (table 1). The current applied to the quadrupole magnets is a monotonically increasing function of beam energy with no discontinuities over the whole range of energies studied (data not shown). Only minor changes in the MFH were measured when setting the beam line magnets. The maximum change in MFH was measured to be less than 2 parts per million (ppm) for a 220 MeV beam at a baseline MFH of 109 ± 1 ppm.

During operation of the scanning magnets at maximum beam energy (220 MeV), a minor change in the central resonance frequency of -0.3 ± 2.1 and 3.7 ± 2.0 Hz was measured for the two extreme spot positions at $(X = 0 \text{ cm}, Y = -12 \text{ cm})$ and $(X = 0 \text{ cm}, Y = 12 \text{ cm})$ in vertical direction, respectively, whereas

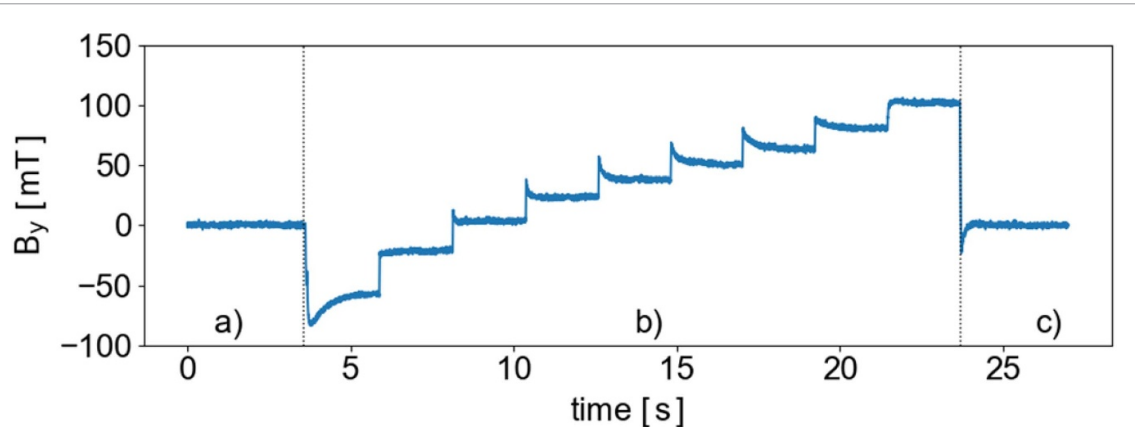


Figure 3. Change in the vertical magnetic fringe field component (B_y) as measured by the tri-axial Hall probe during dose delivery of the X9 spot map. Vertical dotted lines represent the transitions between the time intervals in which the magnets were set to: (a) beam line magnets set for 220 MeV with scanning magnets disabled, (b) operation of the scanning magnets during delivery of the X9 spot map and (c) all beam line and scanning magnets disabled.

the central resonance frequency changed from -90.8 ± 3.5 Hz to 144.0 ± 3.6 Hz for the two extreme spot positions ($X = 24$ cm, $Y = 0$ cm) and ($X = -24$ cm, $Y = 0$ cm) in horizontal direction, respectively. Absolute changes in the MFH were less than 3 ppm for all measurements in both scanning directions.

3.1.2. 3D Hall probe.

Figure 3 shows the time structure of the vertical component of the fringe field (B_y) produced by the scanning magnets during irradiation of the X9 spot map. The spot location dependent effect on the magnetic fringe field that the X-scanning magnet produced for the 220 MeV beam can be appreciated. From the baseline level, a sharp decrease of approximately 80 mT is observed that is related to spot position ($X = 24$ cm, $Y = 0$ cm) of the radiation field. Then, a stepwise increase in B_y takes place every 2.2 s until spot position ($X = -24$ cm, $Y = 0$ cm) is reached. Here, the level of B_y has increased to 105 mT, after which it returns to the baseline level immediately after the 9th dose spot has been delivered. Note that for each change in spot location a transient magnetic field effect of less than 1 s occurs. Hall probe response times, including induction, are below $0.5\ \mu\text{s}$ (Crescentini *et al* 2017), which shows that a transient effect from the measurement device can be excluded. Thus, the observed effect is due to the settling behaviour of the scanning magnet after current ramping caused by eddy currents inside the magnet.

The Y9, Y17, Y33 and Y81 spot maps show a similar stepwise change in B_x with an amplitude between first and last spot of 40 mT, whereas for the Z9 spot map no change is seen in any of the measured field components. This indicates that the Hall-probe resolves fringe field changes due to setting of the scanning magnets, but is insensitive to changes in the settings of the beam line magnets.

3.2. Image quality experiments

3.2.1. Baseline imaging: static beam line settings.

Images from the baseline experiment showed no visual differences between beam line magnets disabled and beam line magnets set for a 220 MeV beam (figure 4), except for a subvoxel shift of less than 0.5 mm in FE direction, which is due to uncertainties in the pre-scan frequency calibration (Schellhammer *et al* 2018a). A similar image quality was achieved with the beam line magnets energized for 70 and 125 MeV. Hence, no visual image degradation was observed due to the static settings of the beam line magnets. Consequently, the dynamic effects of PBS irradiation during imaging could be studied independently in the following.

3.2.2. Imaging and simultaneous volumetric proton beam scanning: dynamic beam line effects.

Images acquired during irradiation of the Z9 spot map showed no visual differences to the images acquired at baseline. The same applies to the Y9, Y17, Y33 and Y81 spot maps. This shows that beam energy variation and vertical beam scanning does not deteriorate the MR image quality.

The MR images acquired during horizontal beam scanning, however, clearly show coherent ghosting artefacts in the PE direction (figure 5). The number of ghosts in the images decreases with increasing number of dose spots applied during image acquisition. The observed effects can be attributed to phase shifts occurring between adjacent lines in k -space. This is evident from k -space phase images (figure 6(a)), which clearly show the nine consecutive time intervals during which k -space was linearly filled while the X9 spot map was delivered.

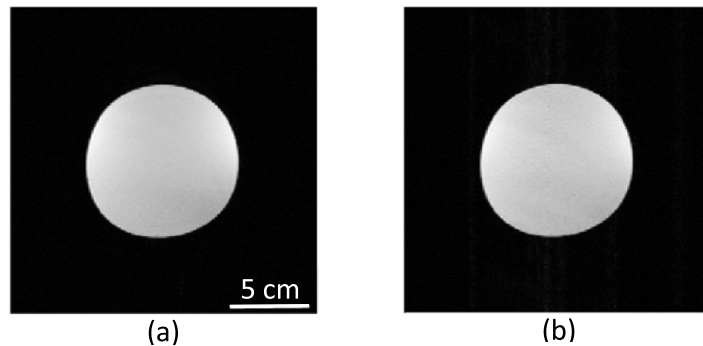


Figure 4. GRE images of an axial slice of the homogenous region of the ACR phantom (a) with all beam line magnets disabled and (b) with the beam transport magnets set for 220 MeV.

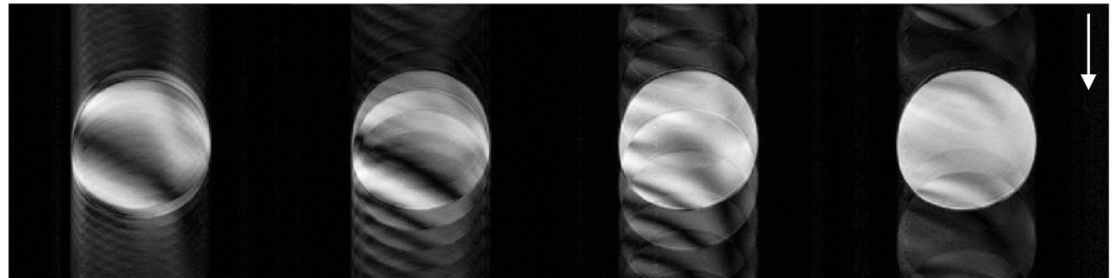


Figure 5. GRE images of an axial slice of the homogenous region of the ACR phantom acquired during irradiation of the X9, X17, X33 and X81 spot maps (from left to right) show the ghosting artefacts in PE direction (white arrow).

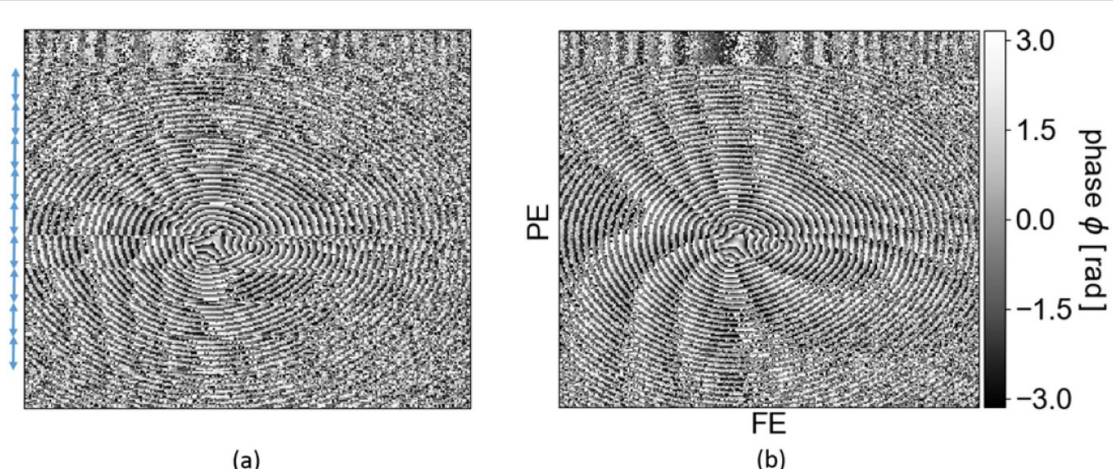


Figure 6. Phase images of the k -space acquired during (a) irradiation of the X9 spot map and (b) at baseline. Blue arrows on the left indicate the time interval (about 25 lines each) of each single dose spot. Since k -space is filled linearly from top to bottom, the first 25 lines represent the dummy scans.

3.3. Computer simulation

The reconstructed MR image and k -space phase map that were synthesized in the computer simulation experiment by k -space phase manipulation of a baseline image are shown in figures 7(c) and (a), respectively. Further, for comparison, figures 7(b) and (d) show the k -space phase and reconstructed magnitude image acquired during irradiation of the X9 spot map. As expected, the simulated and measured images show the same number of ghosts and similar intensity variation inside the circular object imaged. This demonstrates that the presented theory is capable to accurately describe the observed image artefacts.

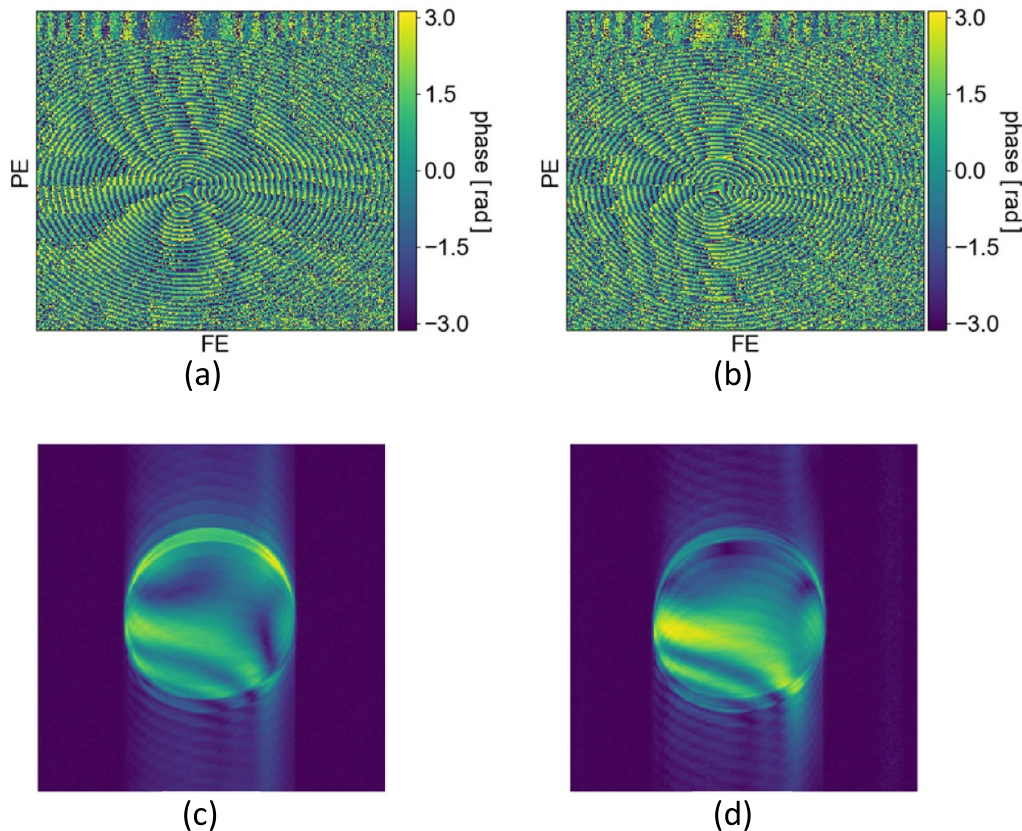


Figure 7. Simulated k -space phase (a) and magnitude (c) image resulting from the computer simulation experiment. Measured k -space phase (b) and magnitude (d) image acquired during irradiation of the X9 spot map.

4. Discussion

For the successful development of MR-integrated PT, artifact-free real-time imaging during proton PBS irradiation is considered an absolute necessity for organ motion tracking and beam gating. We conducted a first systematic experimental investigation into the effects of simultaneous imaging and actively scanned proton pencil beam irradiation by utilizing magnetic field measurements in combination with MR imaging experiments during simultaneous irradiation on our research prototype in-beam MR scanner. These experiments provide a comprehensive understanding of the fringe field effects of the proton beam line onto the imaging capability of this in-beam MR scanner.

Baseline experiments prove that the static operation of the beam line magnets does not compromise the MR image quality independent of proton beam energy. Our results have shown that proton energy dependent settings of the beam line magnets change the MR resonance frequency by 18–50 Hz and have no effect on image quality other than the already known image shift in FE direction (Schellhammer *et al* 2018a), which can be compensated for by a pre-scan frequency calibration to a sub-pixel shift below 0.5 mm.

Dynamic operation of the beam line revealed that changing the proton beam energy in 9 equidistant energy steps from 220 to 140 MeV resulted in a total change in f_{res} on the order of 20 Hz. This corresponds to a change in f_{res} of about 2 Hz between adjacent energy layers. Imaging experiments have shown no degradation in image quality while changing the energy layers. Here it is important to note that the time to change energy layers is about 2 s, which implies that the change in f_{res} does not occur between individual lines of k -space but instead is distributed over about 25 lines, thus resulting in a much lower frequency change per line. Furthermore, since for clinically relevant dose distributions the typically energy layer step size is well below 10 MeV (Alshaikhi *et al* 2019) the effect is further reduced.

For vertical beam scanning along the direction of the B_0 field, the MFC measurements showed a total change in f_{res} of 4 Hz between extreme spot positions of the radiation field. For the Y9 spot map, the spot-to-spot change in f_{res} was well below 1 Hz. Accordingly, the acquired MR images showed no degradation in image quality. Horizontal beam scanning showed a much stronger effect on f_{res} , with a maximum frequency change of 235 Hz between the two extreme spot positions of the radiation field. For the X9 and X81 maps, the spot-to-spot resonance frequency change was on the order of 30 and 3 Hz, respectively.

As the time to change between spots is on the order of 1–2 ms, this change in frequency was expected to result in phase changes between adjacent lines in k -space. Our computer simulation experiments confirmed this presumption by showing that severe ghosting artefacts occurred in MR images that were reconstructed from perturbed phase maps in k -space. MR images acquired during B_0 field perturbations due to the horizontal beam scanning showed the same severe artefacts, with the number of ghosts being dependent on the spot scanning frequency. This is consistent with previous findings showing that the number of coherent PE ghosts increases when decreasing the number of k -space discontinuities (Zhuo and Gullapalli 2006).

Based on the results from the 3D volumetric irradiation experiments we conclude that for frequency changes down to 3 Hz between lines in k -space ghosting artefacts occur, whereas for changes on the order of 1 Hz or below no visual change in image quality as compared to the baseline could be observed. This result agrees well to the study by (Hofman *et al* 2013) that investigated magnetic interaction between an MRI system and a nearby cyclotron and concluded that for T2*-weighted gradient echo imaging blurring in PE direction would occur for phase changes larger than $\text{TE}^* \Delta f = 0.05$. For our case with $\text{TE} = 20$ ms this translates to a frequency change of 2.5 Hz.

The spot maps used in our study were designed to have a simple energy layer and spatio-temporal structure, which allowed us to systematically examine the image artefacts due to dynamic dose spot delivery. For clinically representative spot maps, dose application per energy layer is much faster and the spatio-temporal structure per layer will be more complex. The periodicity inherent in the spot maps used for our study is lost. Consequentially, image blurring along PE direction is expected to occur instead of coherent ghosts that degrade the image quality.

To understand the differences in the magnetic fringe field effects produced by the vertical and horizontal scanning magnets, their geometry and field orientation needs to be taken into account. The main magnetic field of the horizontal scanning magnet is parallel or antiparallel to the B_0 field of the MR scanner, whereas the main field of the vertical scanning magnet is perpendicular to the B_0 field. Addition of a field perturbation parallel to the B_0 vector will result in a larger change in its magnitude than adding a field perturbation of the same strength that is perpendicular to the B_0 vector. Thus, we expect the change in MR resonance frequency to be larger for the superposition of the fringe field produced by the X scanning magnet onto the B_0 field than by that of the Y scanning magnet. Apart from this field superposition, the high magnetic permeability of the magnet's iron flux return yoke could lead to an increase in the absorbed magnetic energy by the external fringe fields. Computer modeling studies are needed to understand the complex magnetic coupling underlying this hypothesis. In addition to this, the horizontal scanning magnet is located downstream of the vertical scanning magnet. Hence, the gap between the magnet poles is wider for the X scanning magnet than for the Y scanning magnet, to allow beams deflected in Y direction to pass (Farr *et al* 2013). This results in a less confined magnetic field and consequently in a stronger fringe field, as confirmed by our Hall probe measurements. Maximum differences in the fringe fields of the horizontal and vertical magnets were 180 mT and 40 mT between extreme spots in horizontal and vertical direction, respectively. The synergistic effect of the scanning magnets' geometry and field orientation explains why the fringe field of the horizontal scanning magnet has a stronger effect on f_{res} than that of the Y scanning magnet, even though their distances from the MR scanner as well as their maximum field strengths are almost the same.

The fact, that the observed image ghosting artefacts originate from phase changes in k -space has been demonstrated by our theoretical considerations and computer simulations. In theory, these phase changes can be deduced from the known time structure of the spot map and the spot-position dependent change in f_{res} . Hence, to compensate for this effect, it would be obvious to reverse the phase changes. However, this would require a synchronization between dose spot delivery and k -space filling, as well as a fast and precise online measurement of the central resonance frequency. Additionally, a generalization of the presented theory should be included to account for frequency changes occurring during acquisition of a single FE line. However, this effect is assumed to be very small compared to the PE ghosting seen in this study.

Other potential measures to eliminate the image artefacts due to the dynamic fringe field of the X scanning magnet would need hardware or software solutions. In the former case, magnetic decoupling between the beam line and the MR scanner should be realized to suppress dynamic perturbations in the B_0 field, whereas in the latter, online or offline image correction strategies should be implemented. For magnetic decoupling both active and passive shielding techniques should be considered. For the latter, magnetic modeling will be the key in ascertaining the effectiveness of such an approach (Whelan *et al* 2018). Online corrections should evaluate the central resonance frequency at every signal acquisition. This can possibly be achieved through a navigator-echo approach (Butts *et al* 1994, McGee *et al* 2000, Li *et al* 2009). Offline corrections are expected to be based on either an optimization process to correct phase errors between PE lines (Broche *et al* 2017) or a deep-learning based image correction approach (Küstner *et al* 2019) based on a large set of corrupted and uncorrupted images. Further research is mandatory to determine which of these measures is most promising.

In this regard, it is important to highlight that the change in central resonance frequency does not only affect the phase along the PE direction in k -space, but has additional effects on the image acquisition, such as a shift in slice position that will be relevant for anatomical imaging. Therefore, magnetic shielding or online frequency evaluation strategies are expected to be potentially advantageous over corrections applied to image reconstruction.

The current study provides first experimental evidence that simultaneous MR imaging and dynamic PBS proton irradiation is not feasible without degradation of image quality. This seems to contradict the conclusion of the only magnetic modeling simulation study present to date (Oborn *et al* 2016). However, this study only investigated the magnetic fringe effects of the scanning magnets of a typical PBS beam line assembly on the B_0 field homogeneity of the 1 T split-bore MRI system of the Australian MRI-Linac program from first principles. Our results are consistent with the findings of this study, in that changes in MFH are small and not relevant for geometrical distortion of MR images. However, the simulation study did not investigate the effects on MR image formation. The results of our study, on the other hand, have revealed that severe image ghosting artefacts originate from the phase changes caused by dynamic perturbations in the B_0 field due to the operation of the X scanning magnets.

Our study is subject to a number of limitations. Firstly, the single-slice GRE sequence was deployed because of its simple pulse structure, which helped to unravel the origin of the ghosting artefacts. Although this sequence provides a generally good compromise between image quality and acquisition speed, its acquisition time of 22 s is too long for real-time imaging. Steady-state free precession (bSSFP) sequences are generally used on hybrid MR-linac systems for 2D cine-imaging, as they provide the necessary acquisition speed, a favorable T2/T1 contrast and high SNR (Scheffler and Lehnhardt 2003, Tyler *et al* 2006, Klüter 2019, Raaymakers *et al* 2017). Typically, bSSFP sequences have repetition times (TR) in the order of a few ms, which allows for single-slice frame rates up to 4–8 Hz. Navigator-echo-based image correction approaches seem unfeasible, as they would prolong the TR and thus reduce the frame rate of bSSFP sequences used for cine-imaging. This would imply that magnetic shielding could be a more promising option to reduce B_0 field perturbations during PBS irradiation.

Secondly, the time resolution of the magnetic field camera was too low to resolve changes in the B_0 field due to the time structure of the spot maps, as the time between dose spots is on the order of 1–2 ms, while the camera has a time resolution of 5 s. Therefore, we investigated the B_0 field changes caused by spot-dependent settings of the scanning magnets in a static operation for each spot individually and used the Hall probe which has a high sampling rate (500 Hz) and was placed close to the scanning magnets to resolve the time structure of the dose spot irradiation.

Thirdly, as the MR scanner is moveable, its absolute position is subject to a re-positioning uncertainty of ± 10 mm in both X and Z direction. However, the influence of this positional uncertainty on both the magnetometry and imaging results were found to be negligible.

A different aspect regarding the integration of MR and PT is the energy-dependent proton beam deflection caused by the static imaging and fringe fields of the MR scanner. Although this is beyond the scope of the current article, reference is made to previous computer simulation studies showing the dosimetric effects of a uniform transversal magnetic field in water phantom and patient geometries (Raaymakers *et al* 2008, Moteabbed *et al* 2014, Hartman *et al* 2015, Fuchs *et al* 2017), as well as the dosimetric effects of realistic MR fringe fields (Oborn *et al* 2015). A first experimental validation showed that magnetic field induced proton beam deflection is accurately measurable and predictable (Schellhammer *et al* 2018b). A recent treatment planning study by (Burigo and Oborn 2019) has demonstrated that beam deflection can be adapted for precisely by intensity-modulated PT in the presence of a realistic inline MR fringe and imaging field. For the experimental setup described in the current work, (Schellhammer *et al* 2018a) has shown that a lateral beam deflection of 2.4 cm, 2.0 cm and 1.3 cm was measured at the magnetic isocenter of the MR scanner relative to the central beam axis for respective beam energies of 70, 125 and 230 MeV. Since we only focus on imaging aspects in the current study, we did not consider beam deflection.

As future MRiPT systems might require an MR scanner to be integrated in a rotating gantry to facilitate beam access to the patient from different angles, the MR magnet design may differ from that of the gantry-less in-beam MRI system used in the current study. Nevertheless, we expect our study's findings to be at least partially transferable to a gantry-based system, as long as its beam line has downstream scanning magnets that have a similar geometry to that used in the current study. A magnetic decoupling of the PBS system and the MRI scanner most probably remains indispensable. However, the optimal MR magnet design is subject to ongoing research. For an inline field orientation with the beam directed parallel to the B_0 field, the magnetic fringe field effects on the MR resonance frequency are expected to be reduced relative to a cross-line orientation with the beam directed perpendicular to the B_0 field, since the fringe fields of both the X and Y scanning magnets would be perpendicular to the B_0 field, as was only the case for the Y scanning magnets in the current study. From a dosimetric point of view, an inline orientation is expected to cause

significant beam rotation, whereas more complex beam deflection and distortions have been reported for the perpendicular orientation (Oborn *et al* 2015). Nevertheless, a recent treatment planning study by (Burigo and Oborn 2019) has shown for the first time that dose distributions to be delivered with state-of-the-art intensity-modulated PT can be optimized to account for the presence of an inline MRI fringe field. This promising result stimulates further research into the technical challenges and developments required to bring the concept of MRIPT into clinical reality.

5. Conclusion

For the first time, the effects of the static and dynamic magnetic fringe fields of a proton PBS beam line on the *in-beam* MR scanner's static magnetic field and on the MR image quality have been measured during simultaneous actively scanned proton pencil beam irradiation and MR image acquisition. Severe ghosting artefacts were observed in MR images acquired during proton beam scanning in horizontal direction only. The ghosting artefacts exhibit a systematic behavior that is related to the time structure of the dose spot map delivered. Computer simulations of MR image formation in *k*-space in the presence of external magnetic cross-talk revealed the origin and nature of these artefacts. Appropriate means for elimination of the artefacts have to be studied and implemented before real-time *in-beam* MR imaging during proton PBS irradiation can be realized.

Acknowledgments

The authors thank Andrea Serra (ASG Superconductors, Genova, Italy) for support with the MR image acquisition, Sebastian Uber (OncoRay, Dresden, Germany) for his help during magnetometry experiments, and Julien Smeets, Andreas Schumann, Martin Hejzlar and Jozef Bokor (Ion Beam Applications SA) for research and technical support.

ORCID iD

Sebastian Gantz  <https://orcid.org/0000-0003-1070-5090>

References

- Alshaikhi J, Doolan P J, D'Souza D, Holloway S M, Amos R A and Royle G 2019 Impact of varying planning parameters on proton pencil beam scanning dose distributions in four commercial treatment planning systems *Med. Phys.* **46** 1150–62
- American College of Radiology 2008 *Phantom Test Guidance for Use of the Small MRI Phantom for the ACR MRI Accreditation Program* (Reston, VA: American College of Radiology)
- Broche L M, Ross P J, Davies G R and Lurie D J 2017 Simple algorithm for the correction of MRI image artefacts due to random phase fluctuations *Magn. Reson. Imaging* **44** 55–59
- Burigo L N and Oborn B M 2019 MRI-guided proton therapy planning: accounting for an inline MRI fringe field *Phys. Med. Biol.* **64** 215015
- Butts K, Riederer S J, Ehman R L, Thompson R M and Jack C R 1994 Interleaved echo planar imaging on a standard MRI system *Magn. Reson. Med.* **31** 67–72
- Crescentini M, Marchesi M, Romani A, Tartagni M and Traverso P A 2017 Bandwidth limits in hall effect-based current sensors *Acta Imeko* **6** 17
- Durand E, Moortele P-F, Pachot-Clouard M and Bihan D L 2001 Artifact due to B0 fluctuations in fMRI: correction using the k-space central line *Magn. Reson. Med.* **46** 198–201
- Farr J B, Dessy F, De Wilde O, Bietzer O and Schönenberg D 2013 Fundamental radiological and geometric performance of two types of proton beam modulated discrete scanning systems *Med. Phys.* **40** 072101
- Fuchs H, Moser P, Gröschl M and Georg D 2017 Magnetic field effects on particle beams and their implications for dose calculation in MR-guided particle therapy *Med. Phys.* **44** 1149–56
- Haacke E M, Brown R W, Thompson M R and Venkatesan R 1999 *Magnetic Resonance Imaging: Physical Principles and Sequence Design* (Hoboken, NJ: Wiley)
- Hartman J, Kontaxis C, Bol G H, Frank S J, Lagendijk J J W, van Vulpen M and Raaymakers B W 2015 Dosimetric feasibility of intensity modulated proton therapy in a transverse magnetic field of 1.5 T *Phys. Med. Biol.* **60** 5955–69
- Hofman M B M, Kuijer J P A, de Ridder J W, Perk L R and Verdaasdonk R M 2013 Technical Note: building a combined cyclotron and MRI facility: implications for interference *Med. Phys.* **40** 012303
- Huang S Y *et al* 2018 Portable low-cost MRI system based on permanent magnets/magnet arrays (arXiv: 1812.10474)
- Ito Y, Yasuda K, Ishigami R, Hatori S, Okada O, Ohashi K and Tanaka S 2001 Magnetic flux loss in rare-earth magnets irradiated with 200 MeV protons *Nucl. Instrum. Methods Phys. Res. B* **183** 323–8
- Klüter S 2019 Technical design and concept of a 0.35 T MR-Linac *Clin. Trans. Radiat. Oncol.* **18** 98–101
- Küstner T, Armanious K, Yang J, Yang B, Schick F and Gatidis S 2019 Retrospective correction of motion-affected MR images using deep learning frameworks *Magn. Reson. Med.* **82** 1527–40
- Li J, Wang Y, Jiang Y, Xie H and Li G 2009 Image correction during large and rapid B0 variations in an open MRI system with permanent magnets using navigator echoes and phase compensation *Magn. Reson. Imaging* **27** 988–93
- Marchand B *et al* 2000 IBA proton pencil beam scanning: an innovative solution for cancer treatment *Proc. of EPAC* pp 2539–41

- McGee K P, Felmlee J P, Manduca A, Riederer S J and Ehman R L 2000 Rapid autocorrection using prescan navigator echoes *Magn. Reson. Med.* **43** 583–8
- Moteabbed M, Schuemann J and Paganetti H 2014 Dosimetric feasibility of real-time MRI-guided proton therapy *Med. Phys.* **41** 111713
- Oborn B M, Dowdell S, Metcalfe P E, Crozier S, Guatelli S, Rosenfeld A B, Mohan R and Keall P J 2016 MRI guided proton therapy: pencil beam scanning in an MRI fringe field *Radiother. Oncol.* **118** S78–9
- Oborn B M, Dowdell S, Metcalfe P E, Crozier S, Mohan R and Keall P J 2015 Proton beam deflection in MRI fields: implications for MRI-guided proton therapy *Med. Phys.* **42** 2113–24
- Oborn B M, Dowdell S, Metcalfe P E, Crozier S, Mohan R and Keall P J 2017 Future of medical physics: real-time MRI-guided proton therapy *Med. Phys.* **44** e77–e90
- Raaymakers B W *et al* 2017 First patients treated with a 1.5 T MRI-Linac: clinical proof of concept of a high-precision, high-field MRI guided radiotherapy treatment *Phys. Med. Biol.* **62** L41–50
- Raaymakers B W, Raaijmakers A J E and Lagendijk J J W 2008 Feasibility of MRI guided proton therapy: magnetic field dose effects *Phys. Med. Biol.* **53** 5615–22
- Scheffler K and Lehnhardt S 2003 Principles and applications of balanced SSFP techniques *Eur. Radiol.* **13** 2409–18
- Schellhammer S M, Gantz S, Lühr A, Oborn B M, Bussmann M and Hoffmann A L 2018b Experimental verification of magnetic field induced beam deflection and Bragg peak displacement for MR-integrated proton therapy *Med. Phys.* **45** 3429–34
- Schellhammer S M, Hoffmann A L, Gantz S, Smeets J, van der Kraaij E, Quets S, Pieck S, Karsch L and Pawelke J 2018a Integrating a low-field open MR scanner with a static proton research beam line: proof of concept *Phys. Med. Biol.* **63** 23LT01
- Schippers J M 2018 Beam transport systems for particle therapy *CERN Yellow Report CERN-2017-004-SP 1* 241–52
- Schippers J M and Lomax A J 2011 Emerging technologies in proton therapy *Acta Oncol.* **50** 838–50
- Tyler D, Hudsmith L, Petersen S, Francis J, Weale P, Neubauer S, Clarke K and Robson M 2006 Cardiac cine MR-imaging at 3T: FLASH vs SSFP *J. Cardiovascular Magn. Reson.* **8** 709–15
- Whelan B, Kolling S, Oborn B M and Keall P 2018 Passive magnetic shielding in MRI-Linac systems *Phys. Med. Biol.* **63** 075008
- Zhuo J and Gullapalli R P 2006 MR artifacts, safety, and quality control *RadioGraphics* **26** 275–97